4-2016

Sensitivity Determination in the CHIPS Neutrino Detector

Eve Adde Chase
College of William and Mary

Sensitivity Determination in the CHIPS Neutrino Detector

A thesis submitted in partial fulfillment of the requirement
for the degree of Bachelor of Science in Physics from
The College of William and Mary

by

Eve Adde Chase

Accepted for Honors
(Honors or No-Honors)

Patricia L. Vahle
Patricia Vahle, Director

Henry Krakauer, Physics

Junping Shi, Mathematics

Williamsburg, VA
April 25, 2016

Sensitivity Determination in the CHIPS Neutrino Detector

Eve Chase

Advisor: Dr. Patricia Vahle

May 11, 2016

Abstract

Through neutrino detection, we strive to provide constraints on various neutrino properties such as δ_{CP} and mass hierarchy. Neutrinos are difficult to detect and require large neutrino detectors with appropriate conditions to determine δ_{CP}. While several neutrino experiments strive to constrain δ_{CP}, additional detectors are necessary to further constrain these parameters. We present a computational model to determine detector sensitivity towards measuring unknown oscillation properties. This model focused on the CHIPS neutrino detector, a low-cost experiment designed to test detector technologies while providing to the wealth of information on neutrino properties. Sensitivity constraints are presented for Δm^2, $\sin^2(2\theta_{23})$, and δ_{CP} at the CHIPS detector.

Contents

1 Introduction

1.1 History of neutrino physics

In 1930, a problem arose in the canonical notion of beta decay, leading to the theoretical prediction of the existence of neutrinos [1]. As understood in 1930, beta decay governs the transformation of an atomic nucleus (A) into a lighter nucleus (B), while releasing an electron in the process, such as

$$A \longrightarrow B + e^{-}. \tag{1}$$

The decay process must follow conservation of energy, such that

$$E = \left(\frac{m_A^2 - m_B^2 + m_e^2}{2m_A} \right) c^2, \tag{2}$$

where E is the constant energy, c is the speed of light, and m denotes the mass for each component of the reaction. Surprisingly, through experimental results of beta decay, the emitted electrons were detected at various energies for multiple decay trials. This variation in electron energy spurred a fury of confusion among physicists, with some proposing a deviation from the law of conservation of energy to explain the discrepancy [1]. Wolfgang Pauli suggested that another particle must be emitted along with the electron to account for the differences in energy. Pauli originally called this missing particle the "neutron", which was later to be renamed the "neutrino", following the 1932 discovery of the more-massive neutron [1]. The presently-accepted beta decay process is

$$n \longrightarrow p^{+} + e^{-} + \overline{\nu}, \tag{3}$$

where a neutron is converted into a proton, electron, and antineutrino.

The neutrino has no electric charge, virtually no mass, and can travel through nearly any obstacle. Neutrinos are produced through radioactive decay and nuclear reactions, such as fusion in stars and fission of radioactive elements. Here on Earth, neutrinos with ideal properties for detection are produced by accelerators. Placing neutrino detectors within the path of a relatively concentrated neutrino beamline (discussed further in Section 3) increases the likelihood of particle interactions, thus adding to the bank of scientific knowledge of neutrino physics. Since Pauli's revolutionary theory of neutrinos, several properties of neutrinos have been discovered such as the neutrino mass (Section 1.2) and neutrino oscillations (Section 1.3), in

addition to the experimental detection of the neutrino itself. However, much is left to be discovered about these elusive particles.

1.2 Neutrino mass

The Standard Model assumes the neutrino is a massless particle. However, in 1998 the Super-Kamiokande Collaboration confirmed that neutrinos have mass, albeit a small mass [2]. Located in Japan's Kamioka Observatory, Super-Kamiokande is a 50 kiloton water Cherenkov detector which studies atmospheric and solar neutrinos, in addition to the occasional neutrino produced in a supernova [2]. Through experimental confirmations for the oscillations of atmsopheric neutrinos, the Super-Kamiokande Collaboration confirmed the existence of the neutrino mass, thus providing the first deviation from Standard Model of particle physics and propagating the push for a reformulation of the Standard Model.

1.3 Oscillations

While it is known that neutrinos have mass, the specific value of the neutrino mass is unknown. Neutrinos have three mass eigenstates and can be additionally characterized by type, called flavor. Neutrinos exist in three flavors - muon, tau, and electron - each with a corresponding flavor eigenstate. A one-to-one mapping does not exist between the three flavor eigenstates and three mass eigenstates, such that one particular neutrino flavor does not correspond to one mass eigenstate. A mixing matrix governs the relationship between flavor and mass eigenstates:

$$|\nu_\alpha\rangle = U^*_{\alpha j}\,|\nu_j\rangle\,, \tag{4}$$

where ν_α represents the flavor eigenstates (ν_e, ν_μ, ν_τ) and ν_j represents the mass eigenstates (ν_1, ν_2, ν_3). U is the Pontecorvo-Maki-Nakagawa-Sakata (PMNS) matrix given by

$$U_{\alpha\beta} = \begin{bmatrix} c_{13}c_{12} & c_{13}s_{12} & s_{13}e^{-i\delta} \\ -c_{23}s_{12} - s_{13}c_{12}s_{23}e^{+i\delta} & -c_{23}c_{12} - s_{13}s_{12}s_{23}e^{+i\delta} & c_{13}s_{23} \\ s_{23}s_{12} - s_{13}c_{12}c_{23}e^{+i\delta} & -s_{23}c_{12} - s_{13}c_{12}c_{23}e^{+i\delta} & c_{13}c_{23} \end{bmatrix} \cdot \begin{bmatrix} 1 & & \\ & e^{i\alpha} & \\ & & e^{i\beta} \end{bmatrix}, \tag{5}$$

where $s_{ij} = \sin\theta_{ij}$ and $c_{ij} = \cos\theta_{ij}$ [3]. The various θ's are called "mixing angles", which have mostly been measured experimentally [4]. The Dirac phase, δ, allows for the possibility of CP violation in neutrino oscillations; this variable is often listed as δ_{CP} (discussed further in Section 1.4.2).

As neutrinos propagate, the probability of it being detected as a particular flavor changes [3]. Through the PMNS matrix, we determine the probability of a neutrino produced as flavor ν_α being detected as flavor ν_β after traveling some distance. For example, if α and β refer to the same flavor eigenstate, the survival probability for neutrino flavor α is

$$P(\nu_\alpha \to \nu_\alpha) = P(\overline{\nu}_\alpha \to \overline{\nu}_\alpha) = \left| \sum_j U^*_{\alpha j} e^{-i m_j^2 L/2E} U_{\alpha j} \right|^2, \tag{6}$$

where L is the baseline distance traveled , E is the neutrino energy, and U is the PMNS matrix [3].

Expanding Equation 6, the ν_μ disappearance channel is modeled as

$$P(\nu_\mu \to \nu_\mu) = 1 - 4\left|U_{\mu 3}\right|^2 \left|U_{\mu 1}\right|^2 \sin^2 \Delta_{32}, \tag{7}$$

where $\Delta_{ij}^2 = \Delta m_{ij}^2 L/4E$ [3]. Mass splitting is denoted as Δm_{ij}^2 and is discussed further in Section 1.4.1. The expected ν_μ disappearance channel is shown in Figure 1.

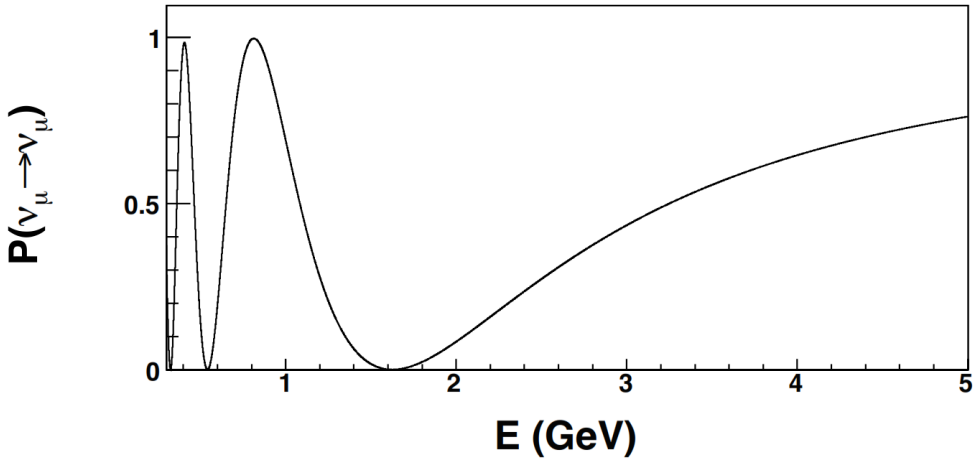

Figure 1: ν_μ disappearance channel for a fixed baseline length L at varying energy [3].

Similarly, we can model muon neutrino to electron neutrino appearance channel, with

$$P(\nu_\mu \to \nu_e) = \left|2U^*_{\mu 3} U_{e3} \sin \Delta_{31} e^{-i\Delta_{32}} + 2U^*_{\mu 2} U_{e2} \sin \Delta_{21}\right|^2, \tag{8}$$

which is approximately equal to

$$P(\nu_\mu \to \nu_e) \approx \left|\sqrt{P_{atm}} e^{-i(\Delta_{32}+\delta)} + \sqrt{P_{sol}}\right|^2, \tag{9}$$

where $\sqrt{P_{atm}} = \sin\theta_{23} \sin 2\theta_{13} \sin \Delta_{31}$ and $\sqrt{P_{sol}} \approx \cos\theta_{23} \sin 2\theta_{12} \sin \Delta_{21}$ [3].

Although first theorized decades earlier, neutrino oscillations were first experimentally confirmed and reported in three papers between 1998 and 2002 [2, 5, 6]. The discovery of neutrino oscillations was a

groundbreaking discovery in physics, leading to the receipt of the 2015 Nobel Prize in Physics to Arthur McDonald and Takaaki Kajita.

1.4 Unknowns in neutrino physics

Neutrino physics has grown immensely in recent decades, and more discovery is imminent. Current and future experiments focus on elucidating properties of mass hierarchy and CP violation.

1.4.1 Mass hierarchy

Although the masses of neutrinos are unknown, we know the differences between mass eigenstates through oscillation studies. In Figure 2, we display the two mass eigenstate configurations, normal hierarchy and inverted hierarchy. Mass splitting is denoted as Δm^2_{ij} which equals $m^2_i - m^2_j$. Atmospheric mass splitting (Δm^2_{atm}) is equivalent to Δm^2_{23} while solar mass splitting (Δm^2_{sol}) related to Δm^2_{12}. We exploit the relationship,

$$\Delta m^2_{31} = \Delta m^2_{32} + \Delta m^2_{21}, \tag{10}$$

and use the values $\Delta m^2_{31} = 2.45 \times 10^{-3}$ eV^2 and $\Delta m^2_{21} = 7.6 \times 10^{-5}$ eV^2.

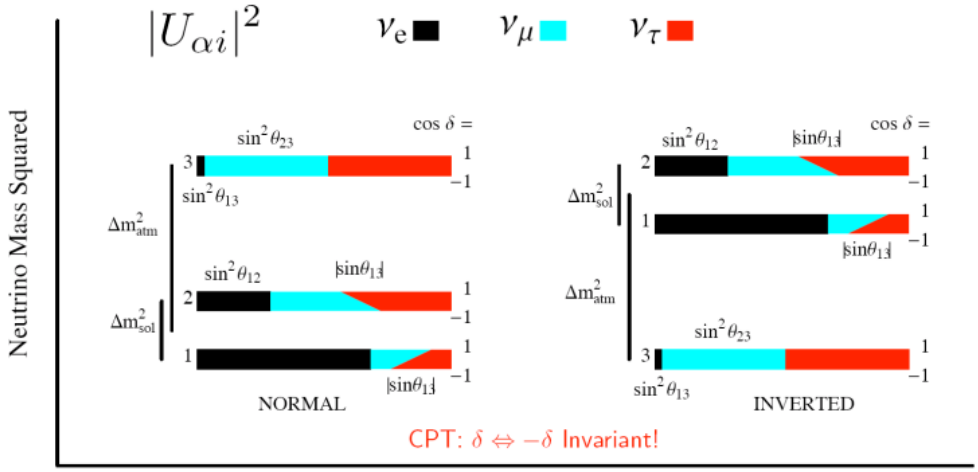

Figure 2: Differences between the normal hierarchy (left) and inverted hierarchy (right) [3].

1.4.2 CP violation

Through the Standard Model, we expect nature to hold an equal parts balance between the amount of matter and antimatter in the universe, but, surprisingly, matter is found to greatly outbalance antimatter. The violation of fundamental particle symmetries, called CP violation, provides a mechanism for this previously inexplicable asymmetry. Small amounts of CP violation have been observed in the quark sector, but not at a level large enough to explain this asymmetry. It is hoped that a large source of CP violation will be observed in neutrino interactions. Particle physicists hope to study CP violation with a large sample size, and neutrino physics may provide this means to better understanding the matter-antimatter imbalance in the universe.

CP symmetry is a combination of charge invariance (C) and parity invariance (P) [1]. CP symmetry refers to an invariance introduced after both charge conjugation (C) and parity (P) are applied. Through charge conjugation, each particle has an associated antiparticle, such as an electron and positron. With parity, a particle is transformed into its mirror image, such as a right-handed particle being converted to a left-handed particle [1]. CP conjugation governs the transformation of a right-handed particle into its left-handed antiparticle and vice versa. A violation of this conjugation symmetry is called CP violation.

By studying neutrino interactions in large quantities, we can elucidate unknown properties of both mass hierarchy and the presence of CP violation in neutrino interactions, as specified by the quantity δ_{CP}.

1.5 Motivation and outline

We compute the sensitivity of a proposed experiment to measure the remaining unknown oscillation parameters in neutrino physics. Throughout this Thesis, we provide the results of these computational models. In Section 2, we provide an overview of the neutrino detection process from long-baseline experiments, with a focus on the CHIPS neutrino detector. In Section 3, we describe neutrino beamline production. Results are presented in Sections 4 and 5. We conclude in Section 6.

2 Detecting neutrinos

Neutrinos are notoriously difficult to detect. Extremely massive detectors, of several kilotons, are used to provide enough matter to induce and observe detectable neutrino interactions. However, at no point during these interactions are the neutrinos detected, themselves. Instead, we detect the byproducts of neutrino interactions with matter; based on properties of these byproducts, we can infer the energy and flavor of the incident neutrino.

A wide range of types and sizes of neutrino detectors have been constructed, including Super-Kamiokande, MINOS, IceCube, and many others. Some detectors primarily detect neutrinos from astrophysical sources, such as supernovae and the Sun, while others detect neutrinos produced through Earth-based accelerators, as described in Section 3. This computational project focused primarily on the CHIPS neutrino detector, as described in Section 2.2.

2.1 Charged current and neutral current interactions

Neutrino interactions can be sorted intro two groups: charged current (CC) interactions and neutral current (NC) interactions. CC and NC interactions both result in a charged lepton and associated neutrino flavor, but exchange a different weak boson in the process. The CC interactions exchange a charged $W^{\pm}$ boson, while NC interaction exchanges a neutral Z^0 boson, as demonstrated in Figure 3. The exchange of a different boson leads to a different leptonic charge of the neutrino produced in either CC or NC interactions. Based on the byproducts of each interaction, CC interactions allow us to identify the flavor of the produced neutrino, while such an identification is impossible for NC interactions [7]. When modeling neutrino events, it is necessary to model both CC and NC interactions.

2.2 CHIPS

A new project, called CHIPS (CHerenkov detectors In mine PitS), is exploring low-cost methods of detector construction, production, and upkeep leading to the deployment of a significantly larger neutrino detector [8]. A prototype detector, shown in Figure 4, has been constructed and deployed in the NuMI (Neutrinos in the Main Injector) beamline, which produces an intense stream of neutrinos originating at Fermilab. Although the prototype detector is not of sufficient size to detect neutrinos, current data is being used to learn how

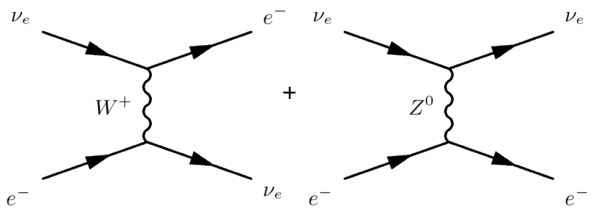

Figure 3: Neutral current interactions exchange a Z^0 boson (right), while charged current interactions exchange a $W^{\pm}$ boson (left) [9]. More generally, a charged lepton and associated neutrino are produced in each interaction, instead of specifically an electron and electron neutrino.

the detector responds to muons from cosmic rays. Eventually, a larger detector will detect NuMI neutrinos.

Figure 4: The CHIPS detector [10].

CHIPS is a Cherenkov detector, a class of neutrino detectors which exploit Cherenkov radiation to detect neutrinos. As a charged particle moving at relativistic speeds passes through a medium, it is possible for the particle to travel faster than the speed of light in that particular medium. This creates light, analogous to a sonic boom. A series of photomultiplier tubes within a neutrino detector can identify and extract information from Chernkov radiation resulting from a neutrino interaction. Cherenkov detectors are typically filled with

water or ice, to provide the medium in which Chernkov radiation can be produced.

The detector is situated 30m underwater in an abandoned northern Minnesota mine pit which has been filled with water [8]. The water from the mine pit acts as a natural shield from cosmic rays, which lead to a source of noise in the detector. While other detectors are located many meters below ground, CHIPS is located at ground-level, leading to a significantly cheaper installation process.

CHIPS provides a playground to explore low-cost technologies and construction procedures to building larger neutrino detectors. Larger and more neutrino detectors are necessary to constrain our understanding of neutrino physics parameters, such as δ_{CP}.

3 Producing neutrinos

In long-baseline neutrino experiments, detected neutrinos are produced in accelerators. In particular, the CHIPS, NOνA, and MINOS detectors interact with neutrinos from the Neutrinos at the Main Injector (NuMI) beamline.

A simplified diagram of neutrino production in the NuMI beamline is shown in Figure 5. To begin, 120 GeV protons interact with a primary target of carbon graphite, which then produces charged pions and kaons at various momenta and angles [12]. These hadrons (pions and kaons) are then focused into a concise beam through two magnetic focusing horns which also sign select charged hadrons in the desired forward direction. Charged pions then enter the decay pipe where they decay into muons and muon neutrinos:

$$\pi^+ \longrightarrow \mu^+ + \nu_\mu. \tag{11}$$

These muons and muon neutrinos then travel through an absorber and lengthy sections of bedrock, which shields the muons while allowing muon neutrinos to pass through. The final product is a relatively concentrated beam of muon neutrinos.

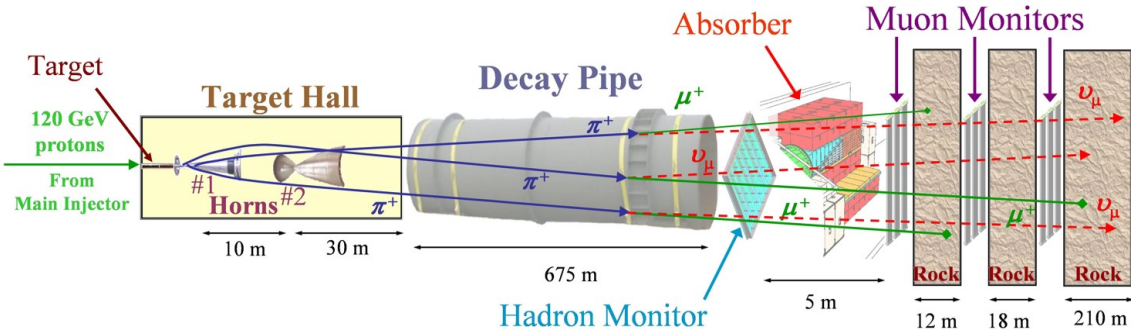

Figure 5: Schematic diagram of the production of a neutrino beamline [11].

Additional attention can be given to the decay processes undergone in the decay pipe, shown in Figure 6. After being focused by the target hall's horns, pions enter the decay pipe at some small angle relative to the central axis. In the lab frame of the pion, the muon and muon neutrino are produced at different angles relative to that of the original pion. The energy of the resultant neutrino is calculated with the following equation:

$$E_\nu = \frac{0.43 E_\pi}{1 + \gamma^2 \theta^2}, \tag{12}$$

where E_π is the pion energy, E_ν is the neutrino energy, γ is the Lorentz factor, and θ is the decay angle between the resultant neutrino and original pion [14]. The neutrino receives an energy "boost" dependent on the decay angle of the neutrino.

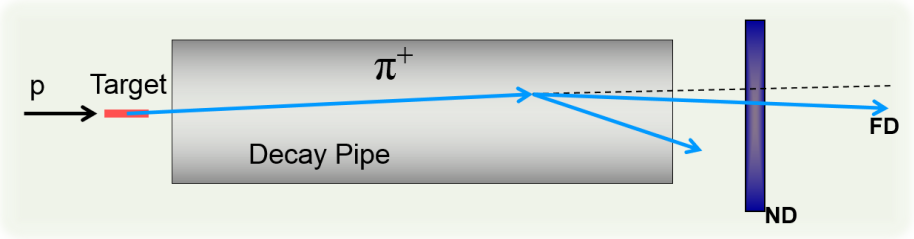

Figure 6: Charged pions decay into muons and muon neutrinos which are later observed at near and far detectors.

Once produced through such a manner, neutrinos travel through many kilometers to various detectors. While our computational study focuses on neutrino properties at the site of the detector, it is imperative to understand the production processes for these neutrinos.

4 Modeling neutrino events

4.1 Code calibration

We begin our sensitivity determination with a previously available code which the NuMI beamline neutrino flux, without taking into account oscillations or higher level effects. This code reads in NuMI beam flux files and calculates the number of neutrinos expected to pass through a unit area of our detector. We incorporate cross section and mass parameters into the flux to create an event energy spectrum. The code takes location input coordinates of latitude, longitude, and altitude of the desired neutrino detector, and outputs an energy spectrum histogram. We reproduce plots using flux files from the NuMI beamline for the CHIPS, NOνA, and MINOS detectors. These detectors are clustered in a similar location in northern Minnesota, but each detector is at a different position with respect to the NuMI beamline (Figure 7). MINOS is directly on axis of the NuMI beamline, while NOνA is far off axis. CHIPS is between MINOS and NOνA at 7mrad off axis, as shown in Figure 7 [8].

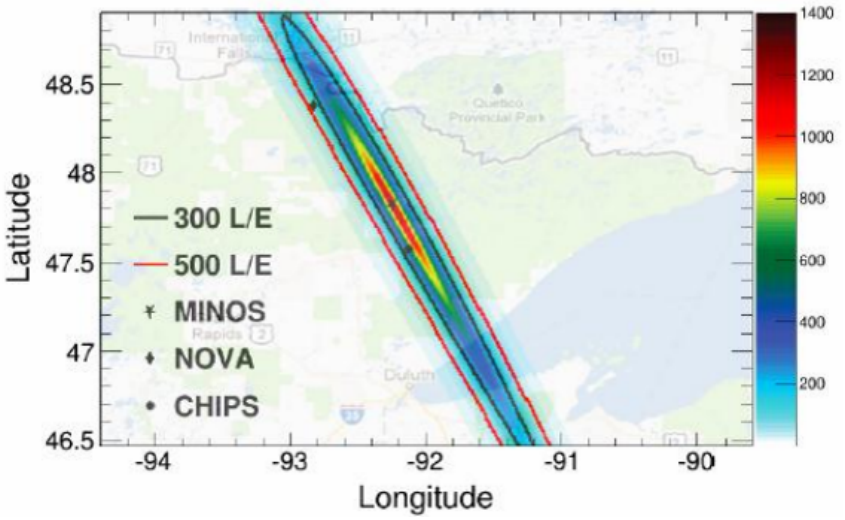

Figure 7: Locations of the CHIPS, NOνA, and MINOS detectors with respect to the rate of neutrino events for the NuMI beamline [8].

It is useful to have both on-axis and off-axis detectors within the path of a neutrino beamline. On-axis detectors, such as MINOS, have maximal neutrino energies, while off-axis detectors, such as CHIPS and NOνA have lower maximum energies, as dictated by Equation 12. The relationship between pion energy (E_π) and neutrino energy (E_ν) is shown for various decay angles in Figure 8. For an on axis detector ($\theta =$

0), pion energy and neutrino energy are linearly related, but this relationship falls for increasingly off-axis detectors. However, these off-axis detectors still provide useful information because interactions at high decay angles are not well understood or documented.

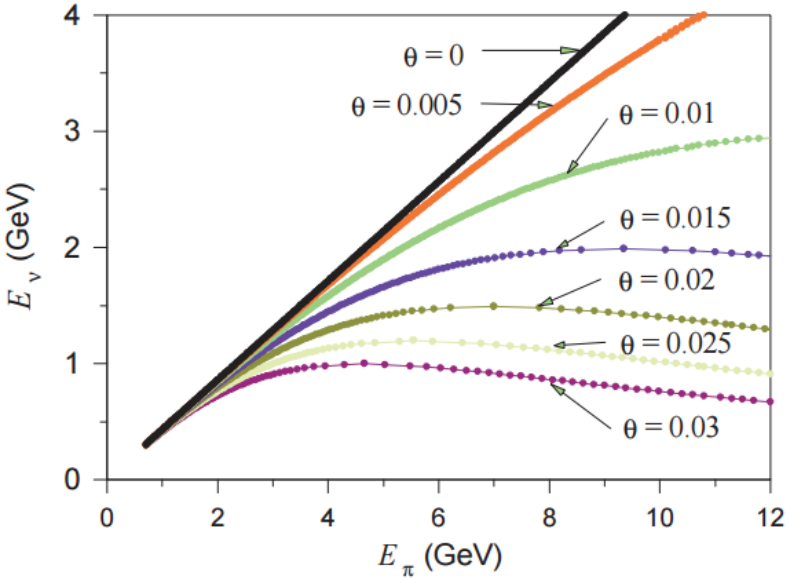

Figure 8: Relationship between pion energy (E_π) and neutrino energy (E_ν) for various decay angles (θ) [14].

Simulated histograms are shown for CHIPS in Figure 9, NOνA in Figure 10, and MINOS in Figure 11. The simulated plots match those expected for all three detectors, providing confirmation for the effective calibration of the code. NOνA, the furthest off-axis detector, has a peak at low energy for the pion decay and a peak at higher energy for kaon decay, which follows an equation similar to Equation 12 but with E_π replaced with the higher energy of kaons.

While the pre-existing code produces expected energy spectra for different geographic locations, the spectra produced are highly idealistic and do not include many physical affects. For example, oscillations and NC interactions are not included in the pre-existing code. Throughout this section, we detail our efforts to include additional neutrino effects into the code and outline steps taken to generate pseudo-experiments, which lead to a more realistic model of expected neutrino events at the site of the CHIPS neutrino detector.

4.2 Inclusion of NC and CC interactions

Without editing the base code, we produced initial plots for ν_μ, ν_e, $\overline{\nu}_\mu$, and $\overline{\nu}_e$, without considering oscillations. Then, we edit the code to simulate both neutral current (NC) and charged current (CC) interactions,

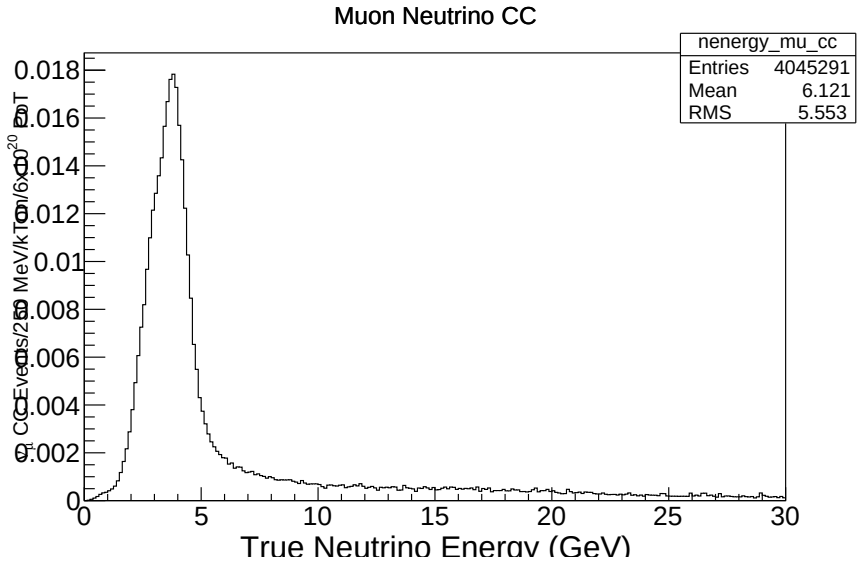

Figure 9: Spectra for ν_μ types over a wide energy range for the CHIPS detector.

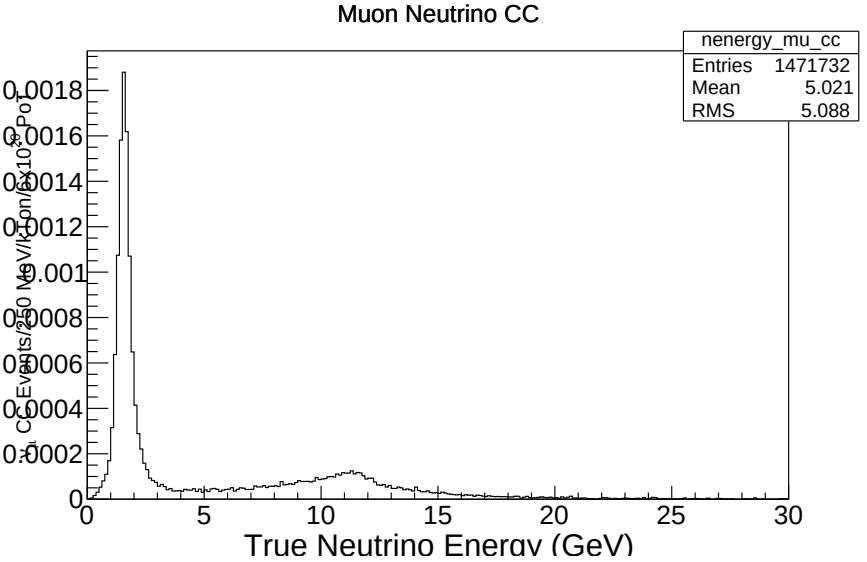

Figure 10: Spectra for ν_μ types over a wide energy range for the NOμA detector.

as outlined in Section 2.1. We update our code to include eight plots: ν_μ, ν_e, $\overline{\nu}_\mu$, and $\overline{\nu}_e$ for both NC and CC. All plots are for the site of the CHIPS neutrino detector. Select plots for spectra of $\overline{\nu}_\mu$ with either NC or CC interactions are shown in in Figures 12 and 13, respectively. All eight plots are shown in Appendix A.

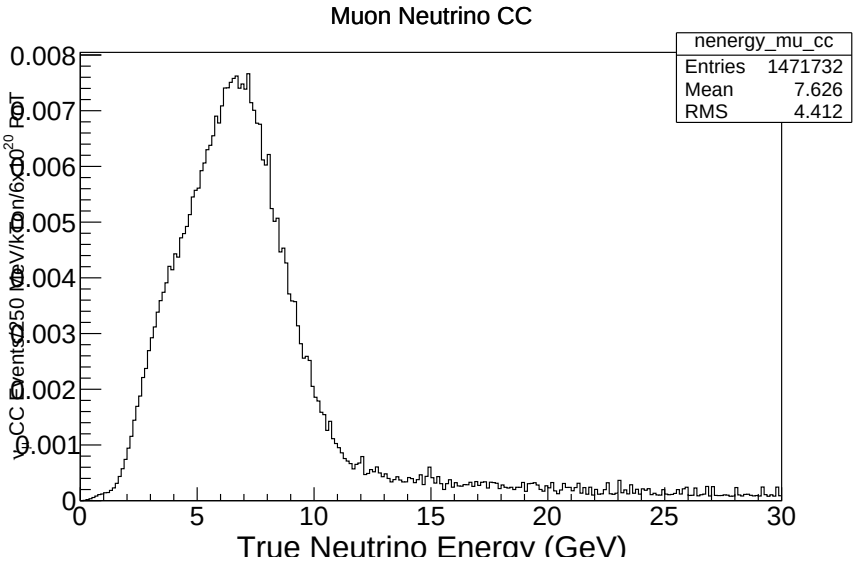

Figure 11: Spectra for ν_μ types over a wide energy range for the MINOS detector.

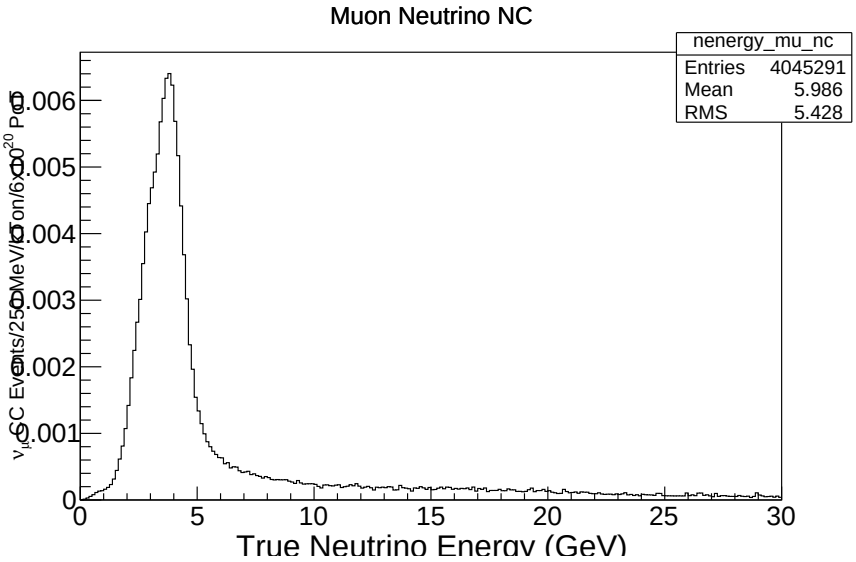

Figure 12: Spectra for ν_μ neutrinos without oscillations for NC interactions.

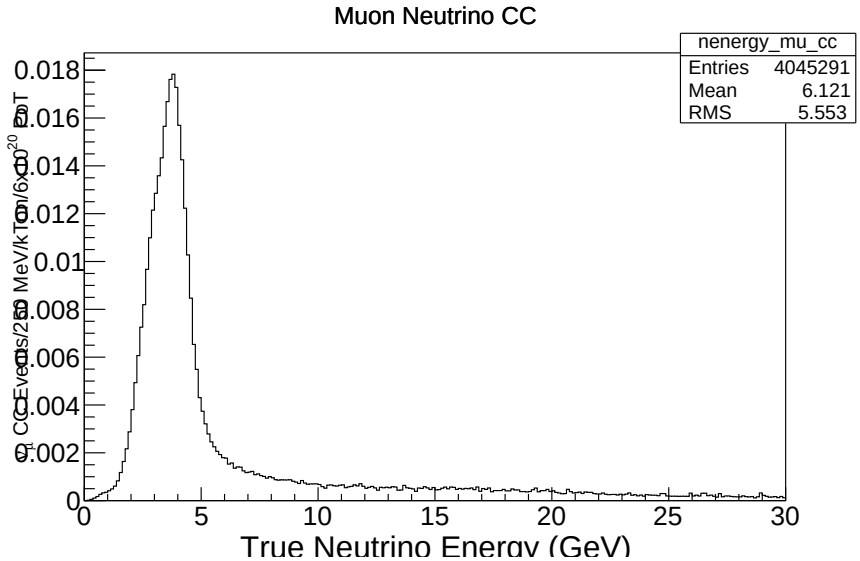

Figure 13: Spectra for ν_μ neutrinos without oscillations for CC interactions.

4.3 Neutrino oscillations

We apply three-flavor neutrino oscillations following a set of equations, enumerated below [3]. The survival probability for a neutrino of flavor α to remain flavor α is:

$$P(\nu_\alpha \to \nu_\alpha) = P(\overline{\nu}_\alpha \to \overline{\nu}_\alpha) = \left| \sum_j U^*_{\alpha j} e^{-im_j^2 L/2E} U_{\alpha j} \right|^2, \tag{13}$$

where L is the baseline distance traveled and E is the neutrino energy. U is the MNS mixing matrix which is enumerated in Equation 5.

We modeled neutrino oscillations for both muon neutrino disappearance and electron neutrino appearance, and incorporated each of these into our code. Muon disappearance follows Equation 7 while electon appearance follows Equation 8. When calculating oscillation probabilities, we use normal hierarchy (see Section 1.4.1), and the following mass splittings:

$$\Delta m^2_{31} = \Delta m^2_{32} + \Delta m^2_{21}, \tag{14}$$

where

$$\Delta m^2_{31} = 2.45 \times 10^{-3} eV^2, \tag{15}$$

and

$$\Delta m^2_{21} = 7.6 \times 10^{-5} eV^2. \tag{16}$$

We use the following mixing angles: $\theta_{12} = 0.593$, $\theta_{13} = 0.1575$, and $\theta_{23} = \pi/4$ [4] and a δ_{CP} of zero.

We have simulated oscillations for ν_μ disappearance ($\nu_\mu \rightarrow \nu_\mu$), and Figure 14 shows the ratio of the ν_μ energy spectrum with oscillations to the spectrum without oscillations. We compare this plot to the expected probability for muon disappearance in Figure 1. Both show similar general trends, with a minimum in probability seen at 1.6 GeV and additional fluctuations at lower energies. Based on the similarities of Figures 1 and 14, in addition to some numerical checks, we conclude that our muon neutrino disappearance oscillations were computed correctly.

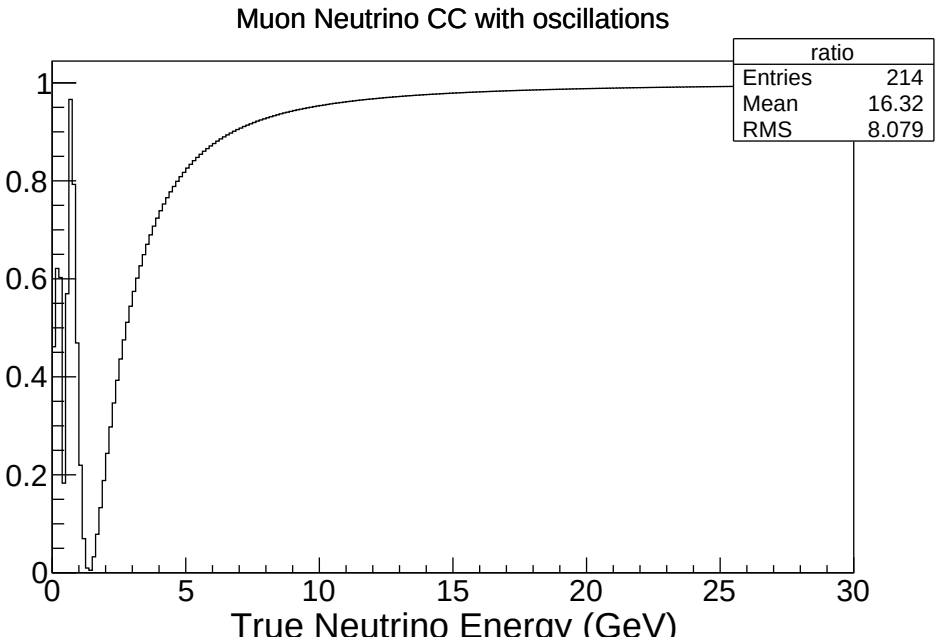

Figure 14: Ratio of ν_μ energy spectrum with oscillations to the spectrum without oscillations, for CC interactions.

Additionally, we have simulated oscillations for ν_e appearance ($\nu_\mu \rightarrow \nu_e$). Figure 16 shows the ratio of the ν_e energy spectrum with oscillations to the ν_μ spectrum without oscillations. At very low energies, the probability for electron appearance rapidly increases to one, which would greatly skew any fitting parameters applied to the histogram as a whole. To resolve this issue, we eliminated all electron neutrino appearance below 200 MeV. We compare our simulated oscillations to those expected from neutrinos with normal hierarchy in Figure 15. Many similar trends are seen, including the peak in probability around 1.4 GeV. Several lower energy probability fluctuations are not seen in the simulated data due to our large bin sizes. Based on these comparisons, we conclude that our electron neutrino appearance oscillations were computed correctly.

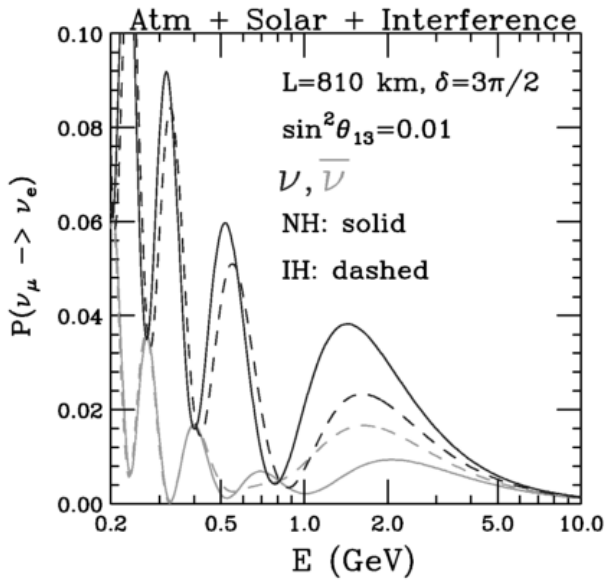

Figure 15: ν_e appearance channel for a fixed baseline length L at varying energy. Black lines show the appearance for neutrinos, while gray lines show comparable effects for antineutrinos. Normal hierarchy is employed in the solid lines, while inverted hierarchy is used in the dashed lines [3].

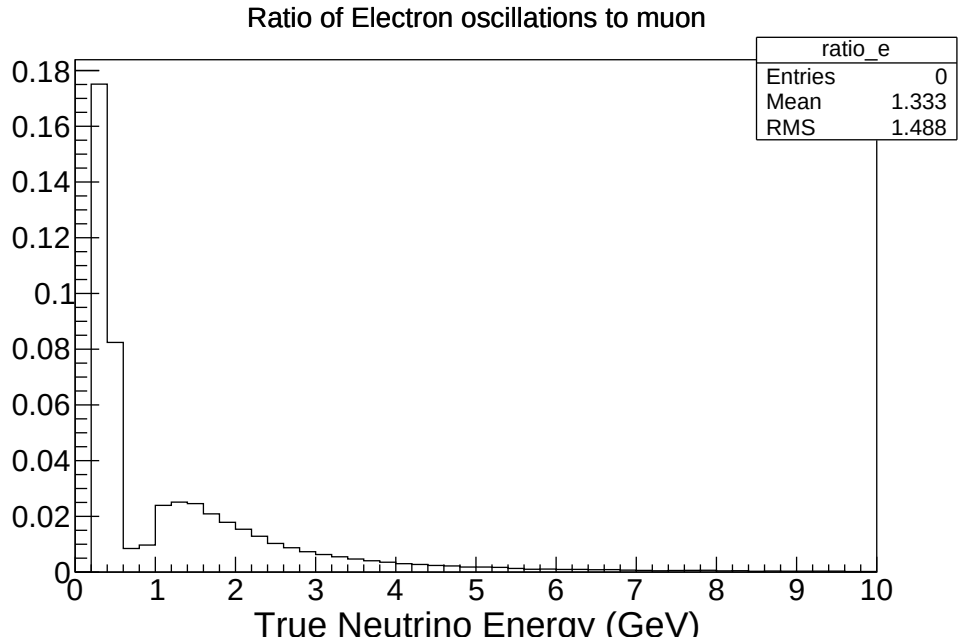

Figure 16: Ratio of ν_e energy spectrum with oscillations tothe ν_μ spectrum without oscillations, for CC interactions.

4.4 Generation of pseudo-experiments

In Figure 17, we show two histograms for ν_μ events, with the black plot representing the histogram without oscillations and the red plot including oscillations. The two histograms share a similar structure, but the peak

flux of neutrinos is reduced by about a third for the oscillated histogram. The two histograms in Figure 17 show idealistic predictions for the expected neutrino detection abilities of CHIPS. These simulations also model over 300,000 expected neutrino detection events, which is highly physically unlikely. As expected from previous neutrino experiments similar to CHIPS, it is assumed that we will see approximately 500 neutrino events. Using statistical simulation methods, we can better approximate a more realistic model for expected neutrino energy spectra.

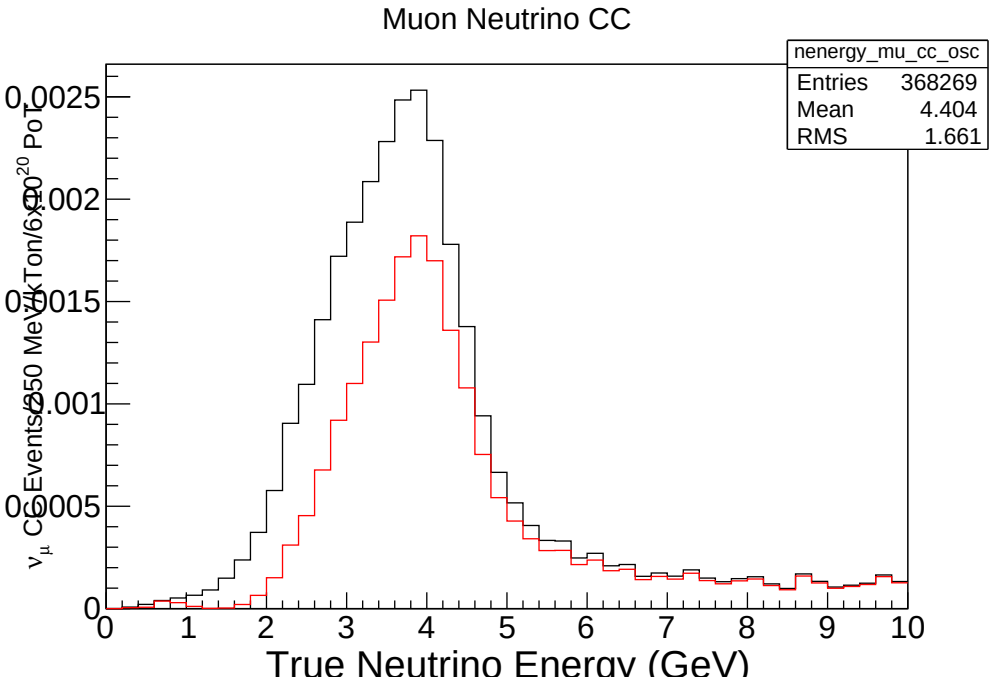

Figure 17: Flux of ν_μ neutrino events with oscillations (red) and without oscillations (black). CC interactions are incorporated.

Using the oscillated histogram, in red in Figure 17, we create similar histograms with random statistical fluctuations. From a Gaussian distribution, we throw a random number N with a mean of 500 and standard deviation of $\sqrt{500}$ to simulate the expected number of neutrino events. Then, we randomly select N events from the oscillated histogram in Figure 17, thus producing a new expected histogram with a smaller number of events. As no single pseudo-experiment is more likely than the others, we generate 10,000 random histograms, called pseudo-experiments. One such pseudo-experiment histogram is shown in Figure 18.

Following an identical procedure, we create 10,000 pseudo-experiments for electron appearance. We select N random events from the oscillated histogram for electron neutrinos, seen in Figure 19. Instead of throwing

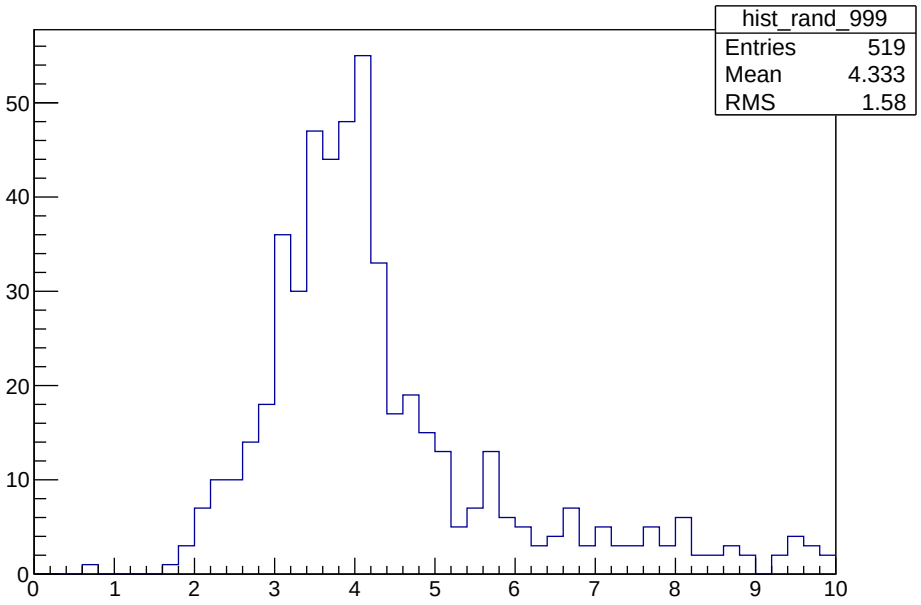

Figure 18: Pseudo-experiment for ν_μ events with 519 events randomly selected from the oscillated histogram in Figure 17. The x-axis shows energy values in GeV while the y-axis counts the number of events in a given energy bin.

a random number with a mean of 500, we randomly select N events with a mean of 39 and standard deviation of $\sqrt{39}$. One of the 10,000 generated pseudo-experiments is shown in Figure 20. It shows many similar trends to Figure 19 but lacks many of the finer features due to the low number of selected events.

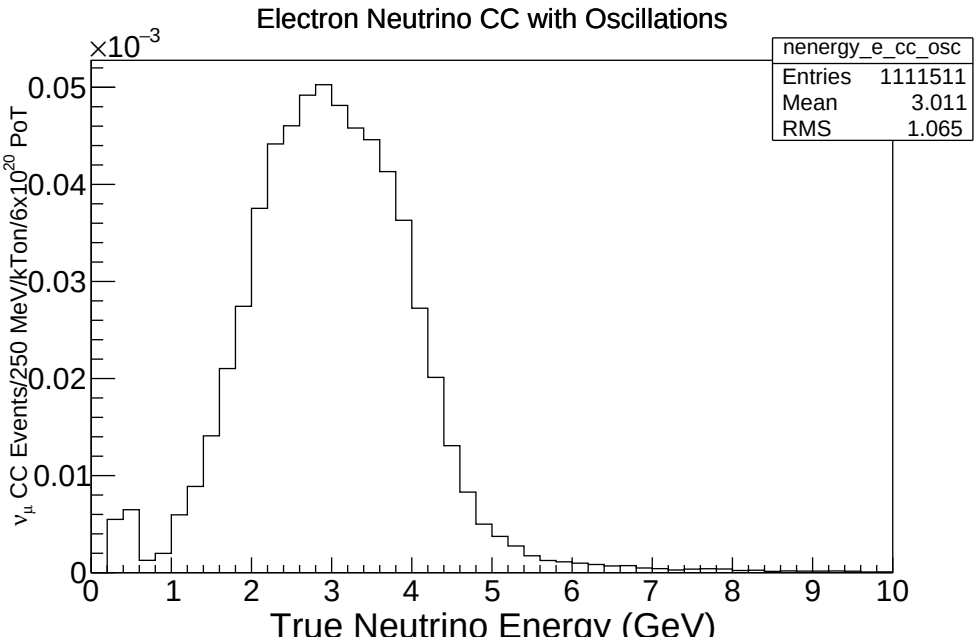

Figure 19: Histogram for ν_e including oscillations, for CC interactions.

4.5 Pseudo-experiment checks

From these stochastic histograms, a series of computational tests are run to check the integrity of our pseudo-experiments. First, we compute a histogram of the number of entries in each pseudo-experiment histogram for muon neutrino disappearance. As seen in Figure 21, the number of entries in the first 1000 pseudo-experiment histograms follows a near-Gaussian behavior with a mean of 501.1, statistically similar to the expected mean of 500. The standard deviation of the data, called RMS on the Figure, is 23.21, which is close to the expected value of $\sqrt{500}$, or 22.36. As I generate the same histogram for more than 1000 pseudo-experiments, the mean and standard deviation get increasingly closer to their expected values. This suggests that our pseudo-experiment algorithm is working correctly.

For an additional check, we add all pseudo-experiment histograms and compare this new histogram to the oscillated histogram in Figure 17. This total histogram in shown in Figure 22. The mean and standard deviation are identical to those in Figure 17 and the plot shares a similar shape to the oscillated histogram.

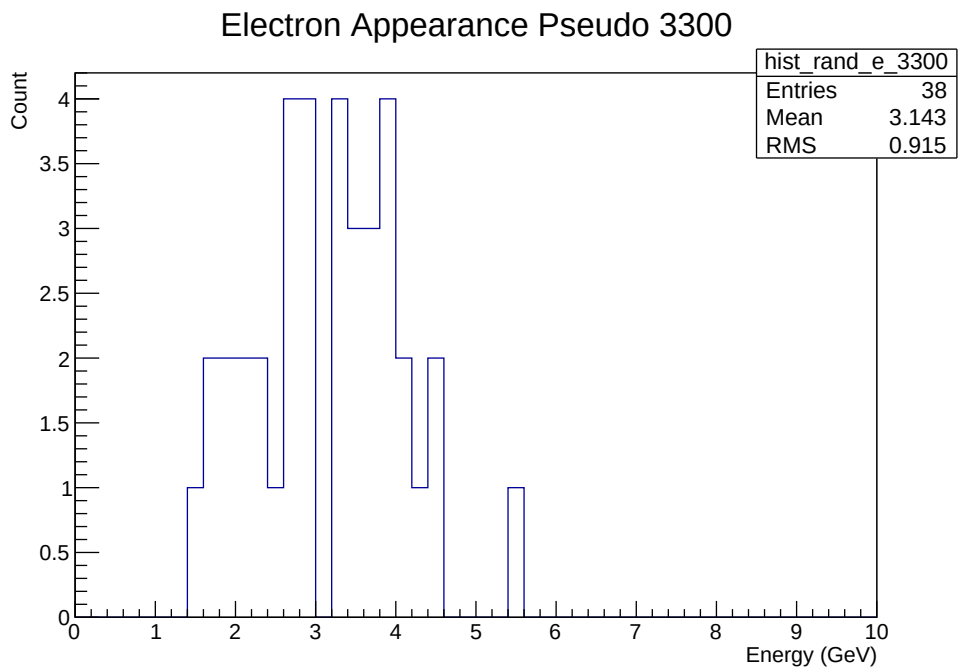

Figure 20: Pseudo-experiment for ν_μ events with 38 events randomly selected from the oscillated histogram in Figure 19.

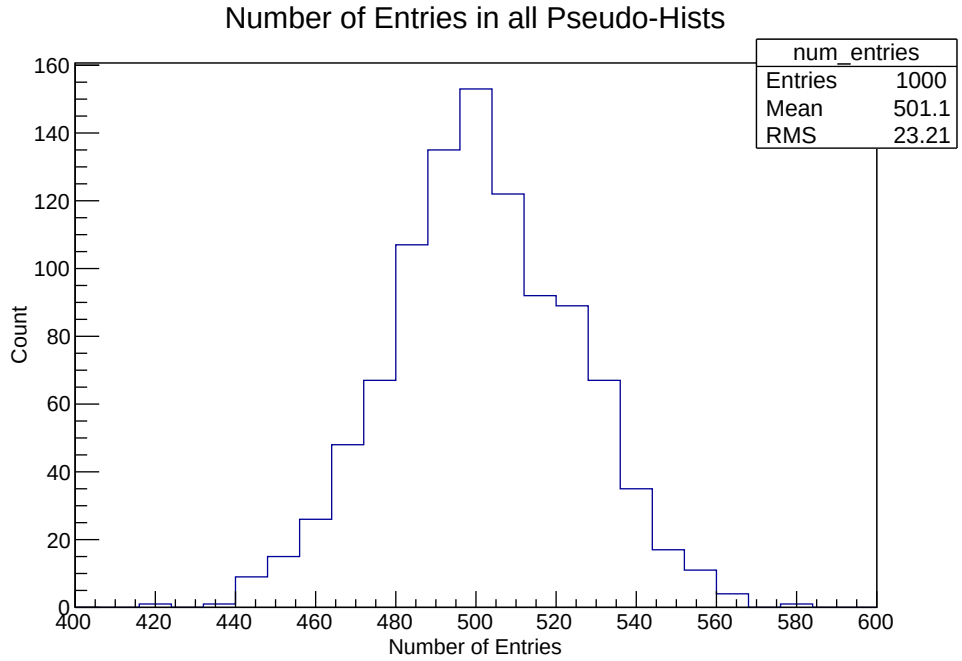

Figure 21: Histogram of number of entries in the first 1000 pseudo-experiment histograms.

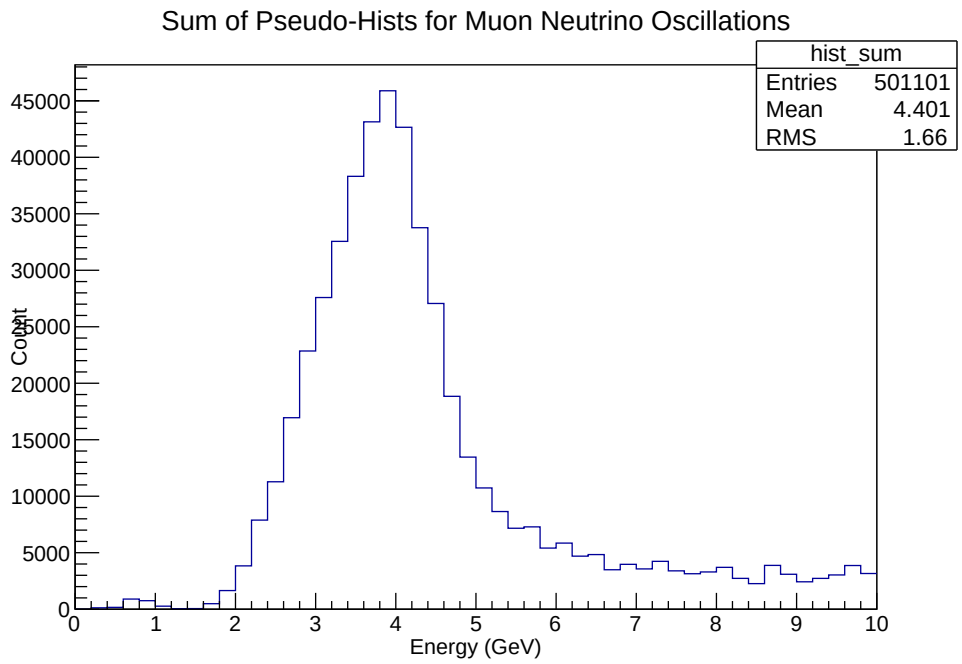

Figure 22: Sum of all pseudo-experiment histograms.

From these two checks, we are confident in the functionality of our pseudo-experiment histogram generation procedure. Since electron neutrino appearance pseudo-experiments were generated with an identical procedure to that of the muon neutrino appearance pseudo-experiments, we assume that the electron neutrino plots are also accurate.

5 Fitting pseudo-experiments

From these pseudo-experiments, we work to create a fit for oscillation parameters which best matches the histograms. We begin our fit procedure for muon neutrino disappearance by taking one random pseudo-experiment histogram and the unoscillated histogram from Figure 17.

For each bin in our histograms (i), we extract the unoscillated histogram value (n_i) and the pseudo-experiment histogram value (ν_i) at the same bin. We loop over all bins computationally, to compute the log-likelihood, in accordance with the following equations:

$$L = -2\sum_{i}^{N}\left(\nu_i - n_i + n_i \ln\frac{n_i}{\nu_i}\right), \tag{17}$$

$$\chi^2 = -2\ln L. \tag{18}$$

We run a χ^2 minimization fit, which in turn maximizes the log-likelihood function, L. After setting some initial start parameters, we call the built-in minimization algorithm which uses our log-likelihood function. This log-likelihood function is then fed into a χ^2 determination. The minimization functions work to find parameters which minimize χ^2, giving us a fit in the process. An initial rudimentary minimizing function, built in to the CERN `ROOT` library, called `SIMPLEX`.

Once this algorithm reports new fit parameters, we then run a higher-level minimization function, called `MIGRAD`, to further tune the parameters, using the most recent minimization parameters as a starting point. The code will then print out the two fit parameters, and make a new histogram based on the pseudo-experiment histogram with a fit. One such fit can be seen in Figure 23. The pseudo-experiment histogram values are shown in blue data points with error bars, and the fit is shown in red. The black histogram is the unoscillated histogram from Figure 17, with a scale factor of 751 applied. We can compare the fit in Figure 23 to the oscillated histogram in Figure 17; both plots have a similar pattern. Qualitatively, it appears that our calculated fit closely matches that expected from the oscillated histogram.

Fits are calculated for all 10,000 muon neutrino disappearance pseudo-experiments and all 10,000 electron neutrino appearance histograms, by fitting corresponding muon neutrino and electron neutrino pseudo-experiments simultaneously. For all fits, correlation appears among the following fit parameters: Δm^2, $\sin^2(2\theta_{23})$, and δ_{CP}. We can observe such correlation by filling two-dimensional histograms while calculating the fits to show relationships between two parameters at a time.

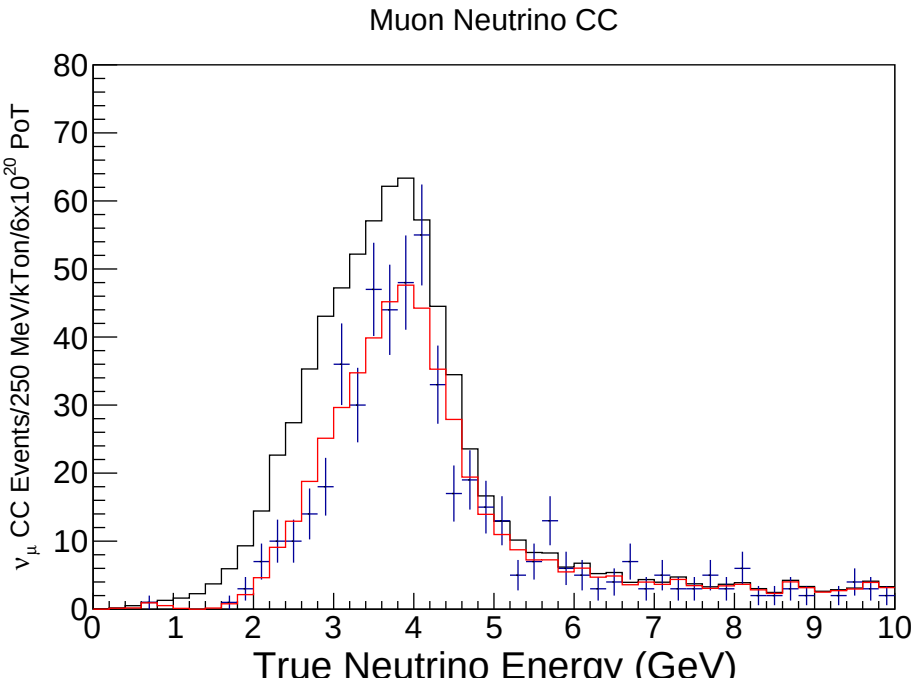

Figure 23: Fit made using the psuedo-experiment histogram in Figure 18, which is shown with blue points with error bars. The black curve is the unoscillated histogram from Figure 17. The red histogram is our fit.

In Figure 24, we show the relationship between Δm^2 and $\sin^2(2\theta_{23})$. Almost all angles are clustered around $\sin^2(2\theta_{23}) = 1$, which suggests maximal mixing. The values for Δm^2 are clustered around 2.5 $\times 10^{-3}$ eV^2, which resembles the assigned value for Δm^2_{31} of 2.45 $\times 10^{-3}$ eV^2. In general, we tend to see expected fit parameters around those that were used in our oscillation calculations in Section 4.3.

In Figure 25, we show the relationship between δ_{CP} and $\sin^2(2\theta_{23})$. Again, $\sin^2(2\theta_{23})$ is clustered around one. However, δ_{CP} is consistently around 5.5, which does not follow the inputted δ_{CP} of zero.

Lastly, in Figure 26, we show the relationship between Δm^2 and δ_{CP}. We see a bimodal distribution, with two clear clusters of fit parameters, with one at a higher Δm^2 and the other at a lower Δm^2 . This bimodal distribution is unexplained and tests have yet to be undergone to explore the relationship between these two parameters.

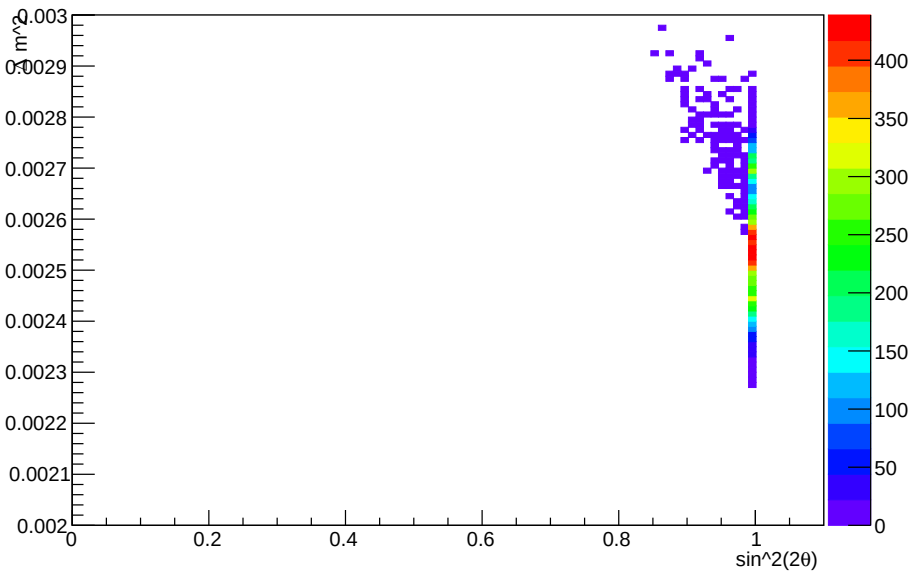

Figure 24: 2D histogram for the relationship between Δm^2 and $\sin^2(2\theta_{23})$. Histogram bins are colored based on occupancy.

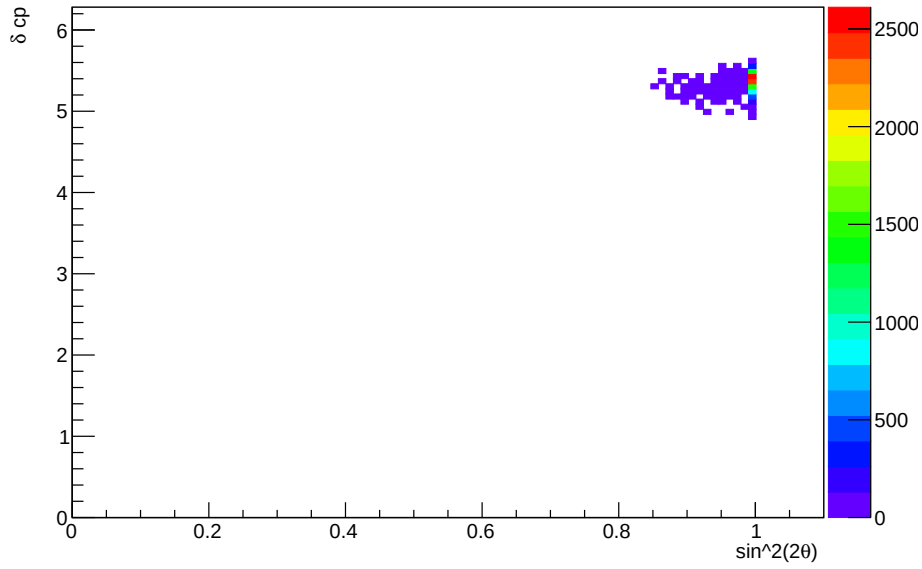

Figure 25: 2D histogram for the relationship between δ_{CP} and $\sin^2(2\theta_{23})$. Histogram bins are colored based on occupancy.

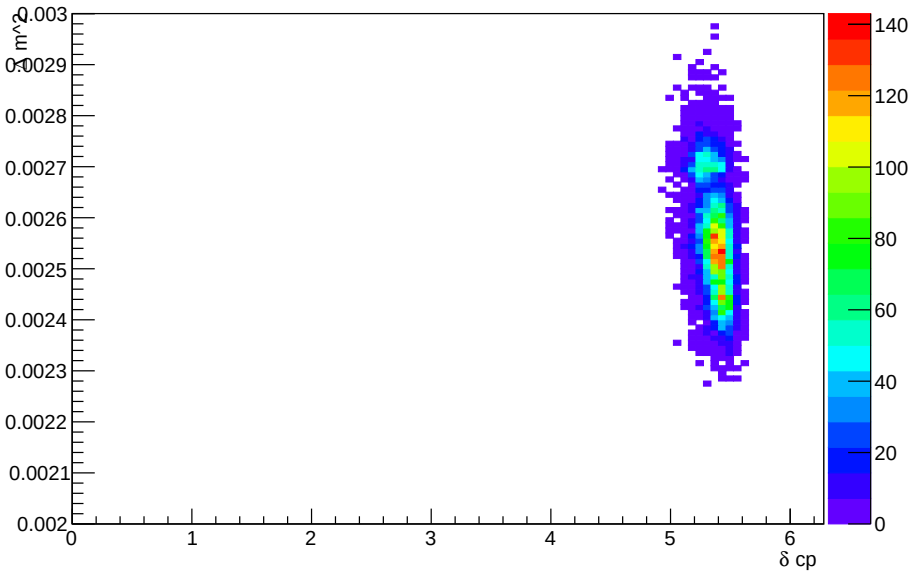

Figure 26: 2D histogram for the relationship between Δm^2 and δ_{CP}. Histogram bins are colored based on occupancy.

6 Conclusion

We have modeled the sensitivity of the CHIPS neutrino detector and its ability to measure remaining unknown oscillation parameters, such as δ_{CP}. We modeled expected neutrino events at the site of the CHIPS detector for ν_μ, ν_e, $\overline{\nu}_\mu$, and $\overline{\nu}_e$ for both NC and CC interactions. In addition, we incorporated three-flavor oscillations for muon neutrino disappearance and electron neutrino appearance into the model.

We began work towards generating a more realistic model of neutrino events expected at the site of the detector, by generating several thousand pseudo-experiments. From these pseudo-experiments, we generated fit parameters to both model expected neutrino events and also determine the relationship and possibility of modeling different fit parameters.

Through the creation of two-dimensional histograms, we observed the relationship between Δm^2, $\sin^2(2\theta_{23})$, and δ_{CP} in our sensitivity model. While Figures 24 and 25 showed the anticipated relationship between fit parameters, Figure 26 showed an unexplained bimodal distribution.

Future work on this project would include a statistical investigation of this bimodal distribution of parameter determination. Additionally, further steps can be taken to create an even more realistic model of detector sensitivity, by including efficiencies and purities into the model.

7 Acknowledgments

I would like to thank Patricia Vahle for help and support throughout this project and for two years of prior research. Additionally, I appreciate the advice and assistance from Jeff Nelson. The original code for this project was provided by Alex Radovic.

References

[1] Griffiths, David. Introductionto Elementary Particles. Wiley-VDH, 1987.

[2] Fukuda, Y. et al. arXiv: hep-ex/9807003v2, 1998.

[3] Parke, Stephen. Neutrino Oscillation Phenomenology. In Jennifer A. Thomas & Patricia L. Vahle, editors, Neutrino Oscillations: Present Status and Future Plans. World Scientific, 2008.

[4] Olive, K. A. et al. (Particle Data Group) Chin. Phys. C, 38, 090001 (2014).

[5] Ahmad, Q. et al. Phys. Rev. Lett. 87, 071301, (2001).

[6] Ahmad, Q. et al. Phys. Rev. Lett. 89, 011301, (2002).

[7] Wang, S. et al. arXiv:1302.1586, 2013.

[8] Adamson, P. et al. arXiv:1307.5918, 2013.

[9] Formaggio, J.A. et al. Rev. Mod. Phys. 84, 1307, (2012).

[10] Meier, J. https://blogs.ucl.ac.uk/science/2014/08/11/picture-of-the-week-dawn-of-the-neutrinos/

[11] Zwaska, R. Fermilab Thesis, 2005.

[12] Milburn, R. H. NuMI-B-109, 1995.

[13] Para, A. & M. Szleper. arXiv:hep-ex/0110032, 2001.

[14] McDonald, K. arXiv:hep-ex/0111033, 2001.

Appendix A Unoscillated histograms

We generate histograms, without oscillations, for ν_μ, ν_e, $\overline{\nu}_\mu$, and $\overline{\nu}_e$ for both NC and CC in Figures 27 - 34.

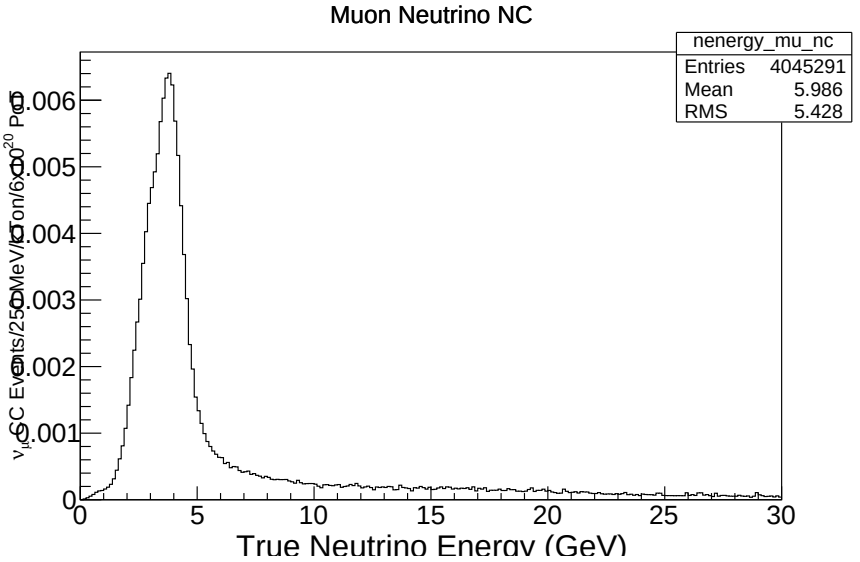

Figure 27: Spectra for ν_μ neutrinos without oscillations for NC interactions.

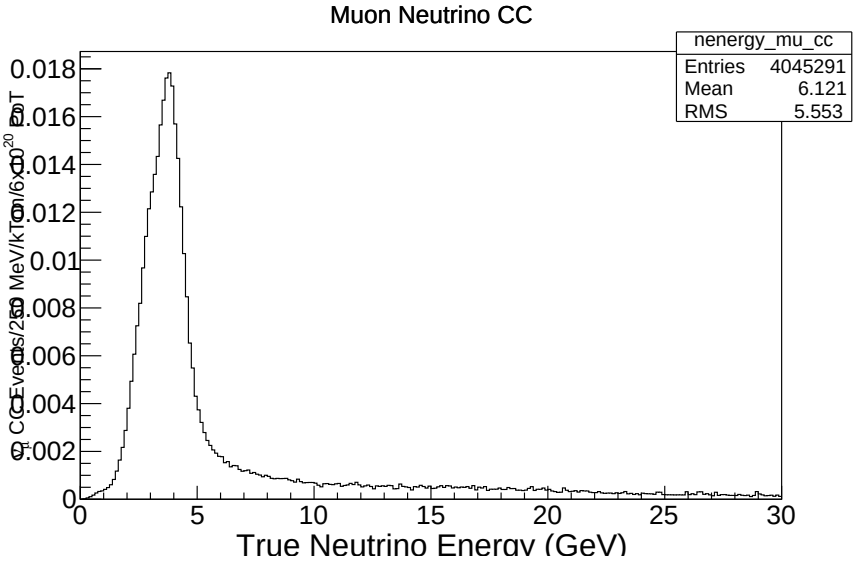

Figure 28: Spectra for ν_μ neutrinos without oscillations for CC interactions.

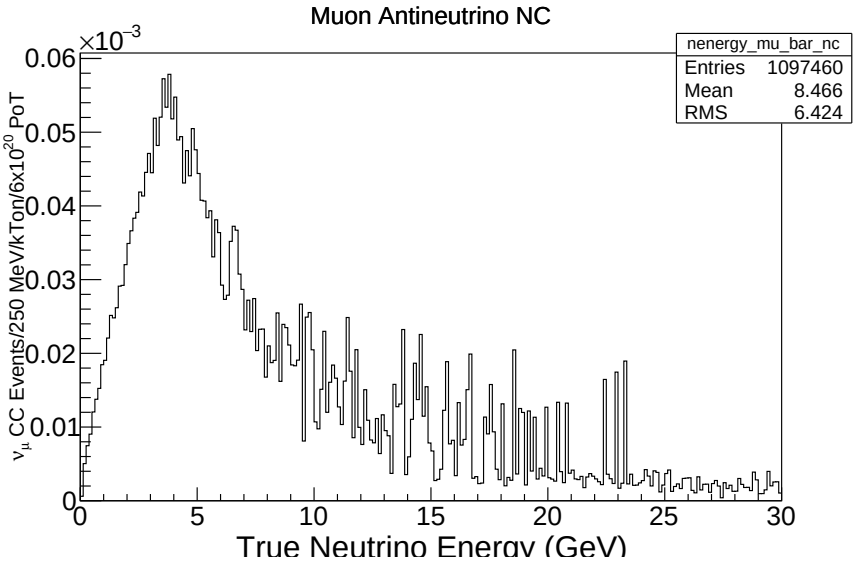

Figure 29: Spectra for $\overline{\nu}_\mu$ neutrinos without oscillations for NC interactions.

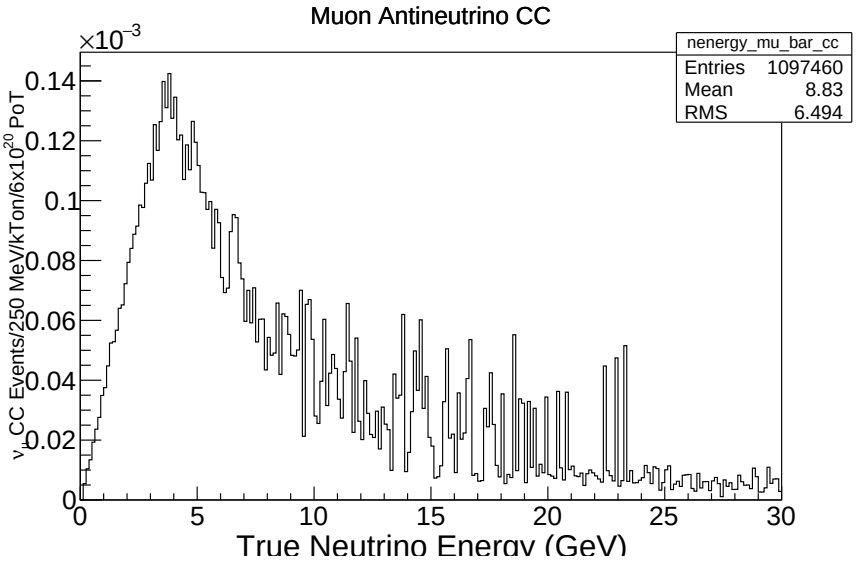

Figure 30: Spectra for $\overline{\nu}_\mu$ neutrinos without oscillations for CC interactions.

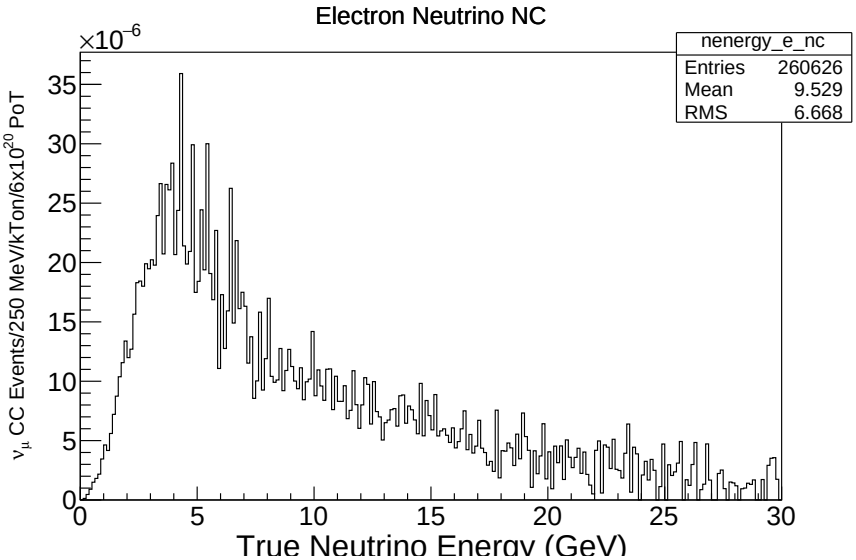

Figure 31: Spectra for ν_e neutrinos without oscillations for NC interactions.

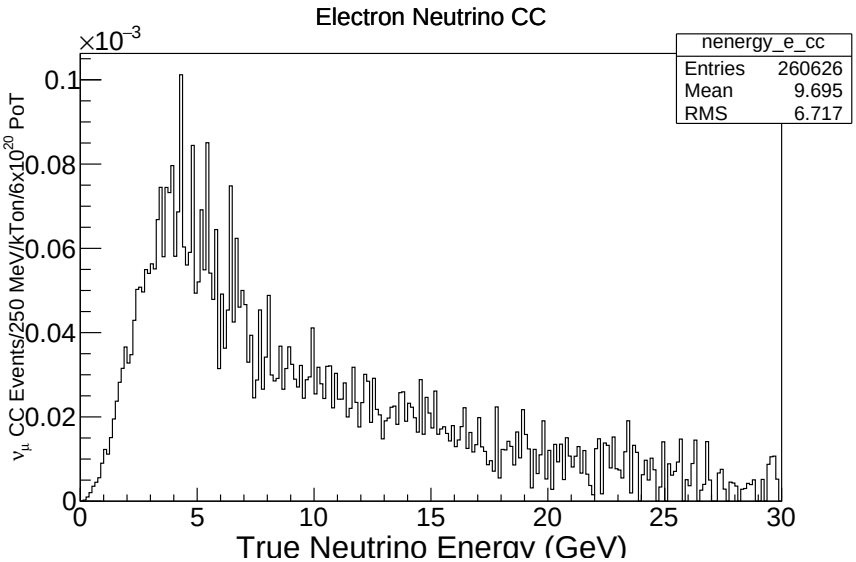

Figure 32: Spectra for ν_e neutrinos without oscillations for CC interactions.

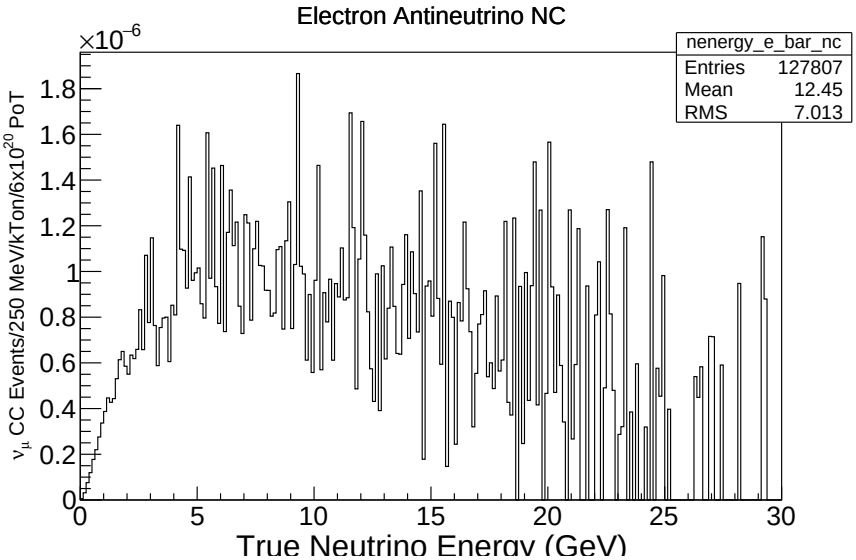

Figure 33: Spectra for $\overline{\nu}_e$ neutrinos without oscillations for NC interactions.

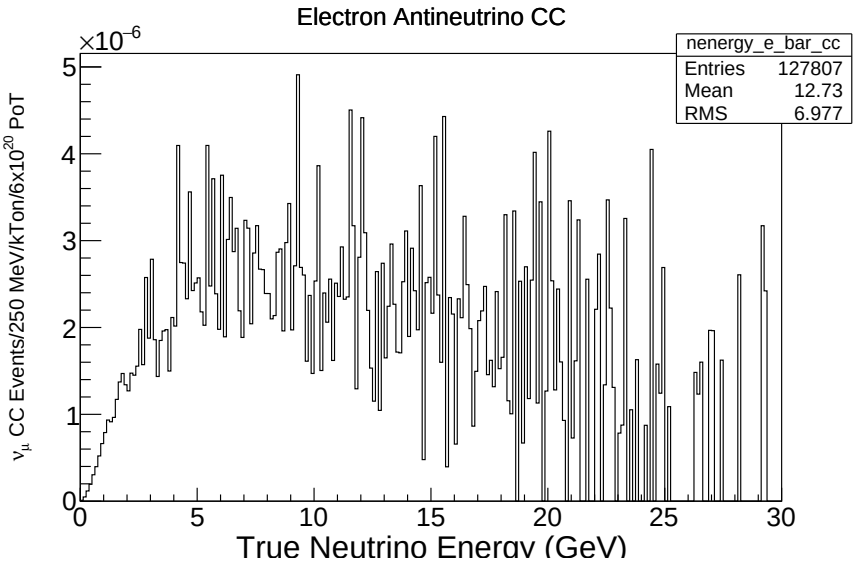

Figure 34: Spectra for $\overline{\nu}_e$ neutrinos without oscillations for CC interactions.